

# ON THE ANGULAR MOMENTUM EVOLUTION OF FULLY-CONVECTIVE STARS: ROTATION PERIODS FOR FIELD M-DWARFS FROM THE MEARTH TRANSIT SURVEY

JONATHAN IRWIN, ZACHORY K. BERTA, CHRISTOPHER J. BURKE, DAVID CHARBONNEAU AND PHILIP NUTZMAN  
Harvard-Smithsonian Center for Astrophysics, 60 Garden St., Cambridge, MA 02138, USA

ANDREW A. WEST

Department of Astronomy, Boston University, 725 Commonwealth Ave, Boston, MA 02215, USA

EMILIO E. FALCO

Fred Lawrence Whipple Observatory, Smithsonian Astrophysical Observatory, 670 Mount Hopkins Road, Amado, AZ 85645, USA  
*Draft version March 29, 2022*

## ABSTRACT

We present rotation period measurements for 41 field M-dwarfs, all of which have masses inferred (from their parallaxes and 2MASS K-band magnitudes) to be between the hydrogen burning limit and  $0.35 M_{\odot}$ , and thus should remain fully-convective throughout their lifetimes. We measure a wide range of rotation periods, from 0.28 days to 154 days, with the latter commensurate with the typical sensitivity limit of our observations. Using kinematics as a proxy for age, we find that the majority of objects likely to be thick disk or halo members (and hence, on average, older) rotate very slowly, with a median period of 92 days, compared to 0.7 days for those likely to be thin disk members (on average, younger), although there are still some rapid rotators in the thick disk sample. When combined with literature measurements for M-dwarfs, these results indicate an increase in spin-down times with decreasing stellar mass, in agreement with previous work, and that the spin-down time becomes comparable to the age of the thick disk sample below the fully-convective boundary. We additionally infer that the spin-down must remove a substantial amount of angular momentum once it begins in order to produce the slow rotators we observe in the thick disk candidates, suggesting that fully-convective M-dwarfs may still experience strong winds.

*Subject headings:* stars: rotation – starspots – stars: low-mass, brown dwarfs – stars: evolution

## 1. INTRODUCTION

The rotational evolution of low-mass stars is predominantly governed by two competing processes. During the pre-main-sequence (PMS) phase, these stars are still collapsing, and thus, the moment of inertia decreases as a function of time. If angular momentum is conserved, the angular velocity must correspondingly increase. This spin-up, which persists until the star reaches the zero age main sequence (ZAMS), is counteracted by angular momentum losses, which are thought to be related to the star-disc interaction at early times (e.g. accretion-driven winds; Matt & Pudritz 2005, or “disc locking”; Königl 1991; Collier Cameron, Campbell & Quaintrell 1995), and stellar winds at late times, particularly after the star reaches the ZAMS.

It is well-established that for solar-type stars, it is possible to reproduce the observed evolution reasonably well within this framework, taking as theoretical inputs a range of disc lifetimes in reasonable consistency with those observed in young clusters, a wind loss law involving saturation of the angular momentum losses past some critical angular velocity  $\omega_{\text{sat}}$  (e.g., Stauffer & Hartmann 1987; Barnes & Sofia 1996), and allowing the radiative core to decouple in angular velocity from the convective envelope (e.g., Krishnamurthi et al. 1997; Allain 1998; Denissenkov et al. 2010). A key feature of this solar-type evolution is that the spread in disc lifetimes gives rise to a

spread in rotation rates in young clusters, with the maximal rotation rate being attained as the stars reach the ZAMS, after which they begin to spin down, and converge toward a narrow range of rotation rates. Around the age of the Hyades ( $625 \pm 50$  Myr from isochrone fitting; Perryman et al. 1998), the convergence is complete and all the stars follow a  $t^{1/2}$  type spin-down thereafter, with rotation rate being a well-defined function of mass and age for F, G and K stars (Barnes 2003, 2007).

Stellar winds depend on the magnetic dynamo that drives field generation, so the magnetic topologies of the stars are important in determining the angular momentum loss rates. For solar-type stars, this is thought to be an  $\alpha\Omega$  dynamo (where  $\alpha$  and  $\Omega$  refer to the “ $\alpha$  effect”, the twisting of the magnetic field lines caused by rotation, and the “ $\Omega$  effect”, driven by differential rotation) operating at the interface between the radiative core and the convective envelope. For a fully-convective star, it is thought that this can no longer operate, and it has been suggested that a turbulent dynamo (Durney, De Young & Roxburgh 1993) or  $\alpha^2$  dynamo (Rädler et al. 1990) may dominate. The former produces small-scale fields that would yield inefficient angular momentum losses through winds.

In recent years, magnetic field measurements of stars on both sides of the fully-convective boundary have become available (e.g., Donati et al. 2008; Morin et al. 2008, 2010; Reiners & Basri 2009). These studies indicate there is indeed an abrupt change in field geometries

moving across the fully-convective boundary, with fully-convective objects storing more magnetic flux in large-scale fields than partially-convective objects. The effect of these changes on winds is not yet clear, but at any rate, we do not necessarily expect that the same wind formalism that works for solar type stars or partially-convective M-dwarfs should necessarily reproduce the observations for fully-convective M-dwarfs.

While several authors have attempted to extend the analysis of rotational evolution to M-dwarfs, and particularly to masses below the fully-convective boundary ( $\approx 0.35 M_{\odot}$ ; Chabrier & Baraffe 1997), the lack of observations in this mass domain has made such an endeavor problematic. While observations in young open clusters have improved dramatically over the last decades, now yielding large samples of rotation periods below the fully-convective boundary (e.g., Stassun et al. 1999; Herbst et al. 2001; Makidon et al. 2004; Lamm et al. 2005; Scholz & Eislöffel 2004a,b, 2005, 2007; Scholz, Eislöffel & Mundt 2009; Cohen et al. 2004; Littlefair et al. 2005, 2010; Cieza & Baliber 2006; Irwin et al. 2007b, 2008a), these extend typically only to a few 100 Myr, and at present only a handful of periods have been measured for older clusters, where the intrinsic faintness of M-dwarfs makes determination of periods difficult. Furthermore, such objects reach the ZAMS at much later ages (a few hundred Myr; Baraffe et al. 1998) than solar-type stars, so older clusters are needed to probe similar stages in the evolution.

Additionally, the Sun has been used in all the studies of solar-type stars as a reference point to tie down the evolutionary models, particularly the normalization of the wind loss law, which relies on having data at late-times. For fully-convective stars, there is as yet no such object: a star with well known mass, age, and a robustly measured rotation period (although Proxima comes closest to providing it; see later in this section). The best progress below the fully-convective boundary toward determining the behavior at late times has been made through  $v \sin i$  observations of field stars (e.g., Delfosse et al. 1998; Mohanty & Basri 2003; Reiners & Basri 2008; Browning et al. 2010). While this information is invaluable, and has led to important insights into the physical processes at play in these stars, it is important to note that  $v \sin i$  observations are not sensitive to the slowest rotators, with typical spectral resolutions yielding a limit of  $3 \text{ km s}^{-1}$ . Due to the small radii of M-dwarfs, this corresponds to rather short rotation periods, e.g. 3.3 days for a  $0.2 R_{\odot}$  star.

Rotation period measurements of field M-dwarfs have provided a few clues as to what might lie below the sensitivity limits of the  $v \sin i$  surveys. Benedict et al. (1998) report a rotation period of 83 days for Proxima Centauri, a star which is highly likely to be fully-convective (they also report a weaker detection of a  $\approx 130$  day periodicity in Barnard's star). Kiraga & Stępień (2007) presented a comprehensive survey of rotation periods for field M-dwarfs, and whilst their sample is limited mostly to objects above the fully-convective boundary (they present periods for two new objects below it), they were able to confirm a long period for Proxima, obtaining 82.5 days. Hartman et al. (2009b) also report a number of long rotation periods for field M-dwarfs from the HATNet transit survey. Finally, we see evidence for a comparably long

rotation period in the transiting exoplanet host GJ 1214 (Charbonneau et al. 2009).

The MEarth transit survey (Nutzman & Charbonneau 2008; Irwin et al. 2009) targets nearby ( $< 33 \text{ pc}$ ) northern hemisphere mid to late M-dwarfs to search for transiting super-Earth exoplanets in the habitable zones of their parent stars. The targets for this survey are selected to have inferred radii  $< 0.33 R_{\odot}$  because this is highly advantageous for a transit survey (Nutzman & Charbonneau 2008), and thus should all lie below the fully-convective boundary. Each star is typically observed at moderate (20 minute) cadence on every clear night for a long period of time ( $\approx 6$  months with the current implementation of the survey). The data therefore possess favorable sampling to search for long rotation periods.

## 2. OBSERVATIONS AND DATA REDUCTION

MEarth is a targeted survey, and thus, has observational properties rather different from the majority of transit surveys. We summarize the salient features in this section, particularly as they relate to the detection of continuous photometric modulations, rather than the discrete transit events for which the survey was designed.

The data for the present work were gathered using all 8 telescopes of the MEarth array, which is located within a single roll-off roof enclosure at the Fred Lawrence Whipple Observatory on Mount Hopkins, Arizona. Data were from two full observing seasons, 2008/2009 and 2009/2010, which run from approximately mid-September to mid-July, where the observatory is shut down during the remaining  $\approx 2$  month period corresponding to the summer monsoon season in southern Arizona. Each star was generally observed during only one of these two seasons, as our target list is cycled annually to increase the sample size searched for transits. During each year of operations, hardware changes were minimal except for necessary repairs, and we used a fixed 715 nm long pass filter combined with a thinned, back illuminated  $2048 \times 2048$  CCD on each telescope. The pixel scale is  $0''.76$  per pixel, yielding a field-of-view of  $26'$  on a side.

Targets for the MEarth survey were selected by Nutzman & Charbonneau (2008) from a subsample of stars from the LSPM-North catalog (Lépine & Shara 2005) with trigonometric parallaxes or spectroscopic or photometric distance moduli indicating they are within 33 pc (Lépine 2005).

For the purposes of this work, it is important to be able to, at a minimum, assign a reliable estimate of mass or spectral type to each target, and produce some estimate of the age. The majority of the MEarth targets are quite poorly characterized from existing data in the literature, often possessing only near-IR JHK magnitudes from the 2MASS all-sky survey, photographic magnitudes from the Palomar Sky Surveys<sup>1</sup>, and proper motion information. We therefore elected to analyze only the  $\approx 1/3$  of the sample with trigonometric parallaxes. There were 273 such stars possessing more than one observation (in practice, more observations are of course needed to detect

<sup>1</sup> Note that although Lépine & Shara (2005) provide V-band magnitude estimates, the majority of these are from photographic plate measurements from the USNO-B1.0 catalog, and therefore have potentially large systematic uncertainties.

a period; the smallest number of measurements for our selected rotation candidates was 207 for GJ 51, see also §3.2). The combined parallax and K-band magnitude information provides one of the best methods to estimate the masses of single field M-dwarfs (Delfosse et al. 2000), and in combination with the proper motion information, can be used on a statistical basis to constrain the Galactic population to which the target belongs, and hence the age. Note that full kinematic information is not available for the majority of our targets as they lack radial velocities, so this population assignment is necessarily quite crude at the present time.

During the night, each telescope observes 20–30 fields, where the vast majority of fields contain only a single target M-dwarf. These are observed sequentially for the entire time they are above airmass 2, cycling around the list to yield a cadence per-field of  $\approx 20$  minutes. Exposure times are selected to yield a signal to noise ratio for the target star sufficient to detect a  $2 R_{\oplus}$  planet transit at  $3\sigma$  per data point, for the assumed stellar radius, which is based on the Delfosse et al. (2000) K-band mass-absolute magnitude relation, and a polynomial fit to the empirical mass-radius data of Ribas (2006) to convert mass to radius.

Basic reductions and light curve generation were performed using an automated pipeline, based on that used by the Monitor project (Irwin et al. 2007a). A number of instrument-specific refinements have been made, and these will be described in full in a forthcoming publication (Berta et al., in preparation), along with our transit search procedures. There are, however, known to be two important systematic effects remaining after this standard processing, which we will now describe as they are important for rotation period detection.

MEarth uses German Equatorial Mounts, which necessitate effectively rotating the telescope through  $180^\circ$  relative to the sky when crossing the meridian. Thus, each target samples two regions of the detector, one for negative hour angle and one for positive hour angle. Flat fielding errors are manifest as different base-line magnitudes on each side of the meridian, so we solve for a “meridian offset” for each object to remove this effect.

Secondly, we discovered correlations between the measured differential magnitudes of the target M-dwarfs and weather parameters, specifically the relative humidity. This effect has been investigated in some detail and will be described by Burke et al. (in preparation). It results from a mismatch in spectral type between the target star and the comparison stars, where typically the comparison stars are much bluer than the targets (usually, they are close to solar-type for the majority of our fields). Variations in the precipitable water vapor (PWV) content of the atmosphere along the line of sight cause the strength of the telluric water vapor absorption in the MEarth bandpass to vary, which affects the photometry of the targets in a way which is not corrected by standard differential photometry procedures (Angione 1999; Bailer-Jones & Lamm 2003). This effect can reach several percent over the course of an observing season for the later M-dwarf spectral types.

Since we lack sufficiently red comparison stars with good signal to noise ratios for the majority of our target fields, we adopt an alternative method to derive the required photometric correction. We create a “common

mode” light curve by taking the median of all of the M-dwarf differential magnitudes observed by all 8 MEarth telescopes in a half hour time bin (where the size was chosen to ensure all stars being observed at a given time are included). The averaging is necessary both to improve the signal to noise ratio, and to remove the effects of any real variability or transits. Since the precipitable water vapor usually varies slowly (the majority of the variations are from night to night) this is sufficient to remove most of the effect. The mismatch in spectral type between the target and the comparison stars varies for each target, and therefore so does the amplitude of the effect, so in practice we subtract a scaled version of the “common mode”, determining the scale factor for each object by standard least-squares methods. The scale factor is generally found to be very well-correlated with the colors (and thus, presumably, spectral types) of the targets.

### 3. PERIOD DETECTION

#### 3.1. Method

In order to properly account for the “common mode” systematic effect and the magnitude offsets between the two sides of the meridian, we adapt the method described in Irwin et al. (2006), which uses least-squares fitting of sinusoids to the observed time-series  $m(t)$ .

We adopt as the null hypothesis a model of a constant (real) magnitude, modulated by the systematics corrections:

$$m_0(t) = \begin{cases} m_- + k c(t), & h < 0 \\ m_+ + k c(t), & h \geq 0 \end{cases} \quad (1)$$

where  $m_-$  and  $m_+$  are separate (constant) baseline flux levels for the two sides of the meridian, and  $k$  is a scale factor multiplying the “common mode”.  $h$  is hour angle, and  $c(t)$  is the “common mode”, determined from a time-binned median of all the M-dwarfs being observed by MEarth at any given moment. The scale factor  $k$  allows for the variable amplitude of the “common mode” component in each M-dwarf due to the differing spectral type mismatch of our targets and comparison stars.

This null hypothesis is compared to the alternate hypothesis that the light curve contains a sinusoidal modulation, again modulated by the systematics corrections, of the form:

$$m_1(t) = \begin{cases} m_- + k c(t) + a \sin(\omega t + \phi), & h < 0 \\ m_+ + k c(t) + a \sin(\omega t + \phi), & h \geq 0 \end{cases} \quad (2)$$

where  $a$  and  $\phi$  represent the semi-amplitude and phase of the sinusoid, and  $\omega = 2\pi/P$  is the angular frequency corresponding to rotation period  $P$ . In order to determine  $\omega$ , we fit this model using standard linear least-squares, at discrete values of  $\omega$  sampled on a uniform grid in frequency from 0.1 to 1000 days. By comparing the best-fitting  $\chi^2$  values for the two hypotheses as a function of frequency, we derive a “least-squares periodogram” that accounts for the effect of the systematics.

Due to the small sample size, we omitted the cut in  $\chi^2$  improvement used by Irwin et al. (2006), and simply subjected all of the light curves to visual inspection, to define the final sample of periodic variables, although in practice all of the objects selected pass the  $\Delta\chi^2_p > 0.4$  criterion used by Irwin et al. (2006). 41 light curves passed this selection, where the remainder were consistent with

no detectable variation, had excessive systematics, or had insufficient data to determine a period. A number of objects appeared to have monotonic trends in time, but it is not clear for many of these if they are due to systematics or to variability at present.

### 3.2. Sample properties

Figure 1 summarizes the overall properties of the sample of 273 stars on which the period search and selection of rotation candidates was performed. As discussed in §2, all of these stars have trigonometric parallaxes, and Figure 1 shows that all of the objects selected as rotation candidates also have more than 200 data points taken on  $\geq 10$  nights (for all but one object on  $\geq 28$  nights), spanning at least 120 days.

It is important to note that the selection we have performed does not remove close binaries from the sample. Tidal effects will modify the rotation rates of the components of such binaries, by transferring angular momentum between the stellar spin and the binary orbit. The dependence of tides on binary semimajor axis is very strong (e.g. Zahn 1977) so the objects showing the largest tidal effects will be in the shortest period systems. It is therefore possible that some of the objects in the present sample have had their rotation rates altered by a binary companion, with the objects rotating at shorter periods being more likely to have been affected.

We also note that the use of K-band absolute magnitude to estimate masses means that these masses will be overestimated for any unresolved binary or multiple star systems due to the extra light from the companion(s).

These issues are best resolved by performing spectroscopic follow-up at high resolution, to search for double-lined objects and for radial velocity variability in order to identify any spectroscopic binaries. This has not yet been done for the present sample, and it is important to bear the caveats discussed in this section in mind in the interpretation of the rotation periods we measure.

### 3.3. Effect of the “common mode” correction

Since we are solving for the “common mode” amplitude simultaneously with the sinusoidal variability, it is important to evaluate the effect of this correction on our period sensitivity.

Figures 2 and 3 show periodograms of the “common mode” light curve, calculated in the same way as those we use for period detection by least-squares fitting of sinusoids. The dominant power in the “common mode” is on long timescales, and at the corresponding  $1 \text{ day}^{-1}$  alias frequencies, with the highest peaks for the two years of observations corresponding to periods of 25.1 days for 2008/2009 and 14.5 days for 2009/2010.

The presence of power at such frequencies could affect our sensitivity to rotation periods in this range. We therefore proceed in the next section to simulate the full end-to-end period detection process, including the effect of the “common mode” and of the visual inspection stages, to evaluate the survey sensitivity.

### 3.4. Simulations

In order to evaluate the sensitivity in period and amplitude, simulations were performed following the method detailed in Irwin et al. (2006), injecting sinusoids with

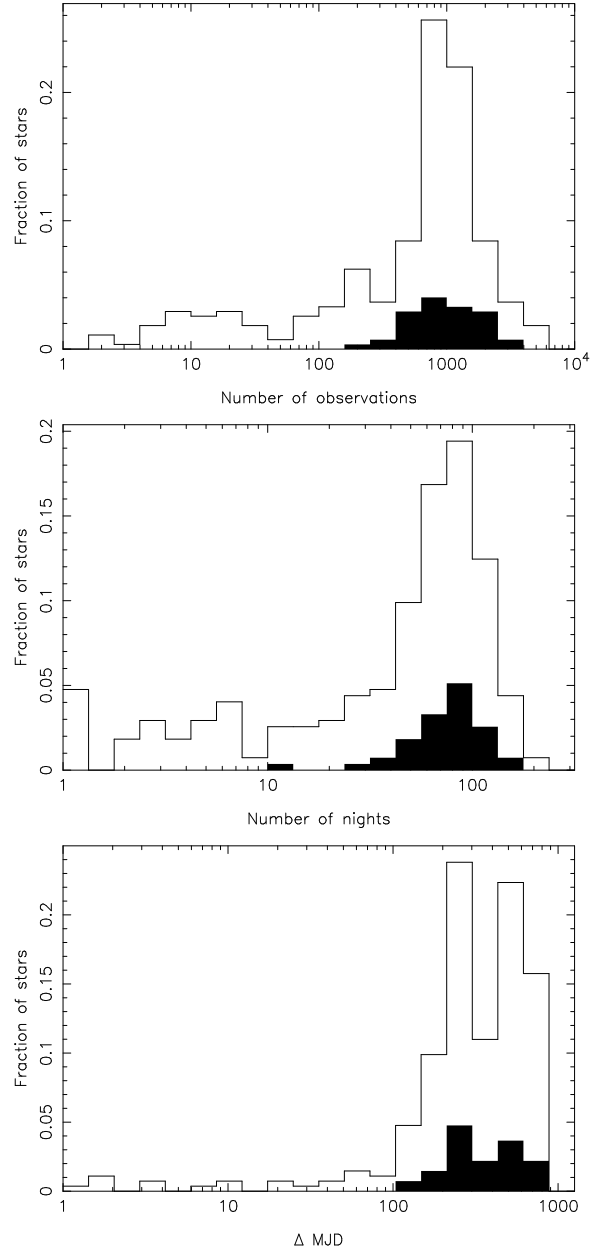


FIG. 1.— Summary of sample properties. In each panel, the open histogram shows the full sample of 273 stars with more than one observation, and the solid histogram shows the 41 stars for which we detect periods. The panels show the number of observations for each target (top), number of nights during which data were gathered (center), and the range of Julian dates spanned by the observations (bottom).

periods from 0.1 to 200 days following a uniform distribution in log period into only the light curves rejected in the previous visual inspection stages to reduce contamination by any real variability. Two semi-amplitudes were simulated, 0.005 and 0.01 mag, corresponding to the range of typical amplitudes of our rotation candidates.

The results are summarized in Figures 4 and 5 for the 0.005 and 0.01 mag semi-amplitudes, respectively. We also show plots of the recovered period versus injected period, in Figures 6 and 7, respectively. Whilst the overall completeness of rotation period detections is quite low (around 50 – 60% in most period bins), there is no clear bias except in the longest-period bin, where the com-

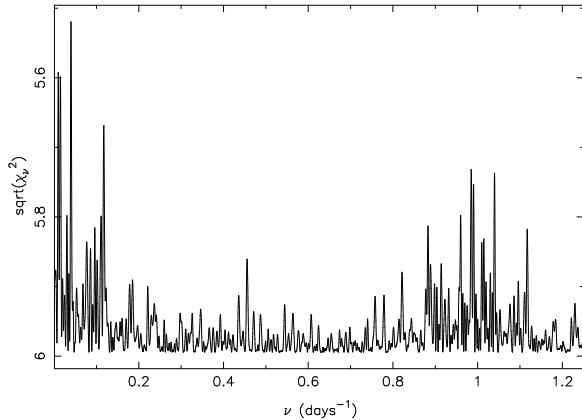


FIG. 2.— Periodogram of the “common mode” light curve for the first year of observations. Plotted as the square root of the reduced  $\chi^2$  of the sinusoidal fit as a function of frequency, with the vertical axis inverted such that higher peaks correspond to more significant detections as for a conventional periodogram. The period of the highest peak is 25.1 days. When computing the  $\chi^2$  values we used the scatter in each time-bin to compute the weights; this appears to significantly underestimate the scatter between the bins, hence the large values of the reduced  $\chi^2$ . The peaks around  $1 \text{ day}^{-1}$  appear to be caused by aliasing, and probably do not represent real variations in the PWV on these timescales. This has been confirmed by analyzing contemporaneous GPS-based PWV measurements (which are not restricted to hours of darkness) from Flagstaff, Arizona.

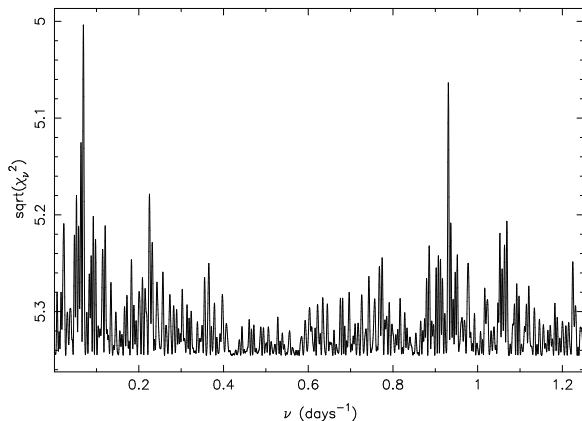


FIG. 3.— As Figure 2 only for the second year of observations. The period of the highest peak is 14.5 days.

pleteness drops to 25 – 30%. This is expected due to the limited survey duration.

The reliability and contamination histograms, and Figures 6 and 7 provide an indication of the reliability of period recovery in the cases where a significant modulation was detected. For 0.01 mag, these statistics indicate very good period recovery, with reliability (measuring the fraction of objects detected with the correct period) above 80% in all period bins, and contamination below 20%. For 0.005 mag the performance is substantially worse, with a large drop in reliability around 1 day and in the longest-period bin. The contamination statistic shows a similar effect. By examining Figure 6, it is clear that some of the scattering of objects in and out of the 1 day bin is due to aliasing, and this diagram also indicates that many of the “incorrect periods” contributing to the poor performance for the longest periods simply have larger period errors than our 10% threshold. This is probably the reason for the apparently small change

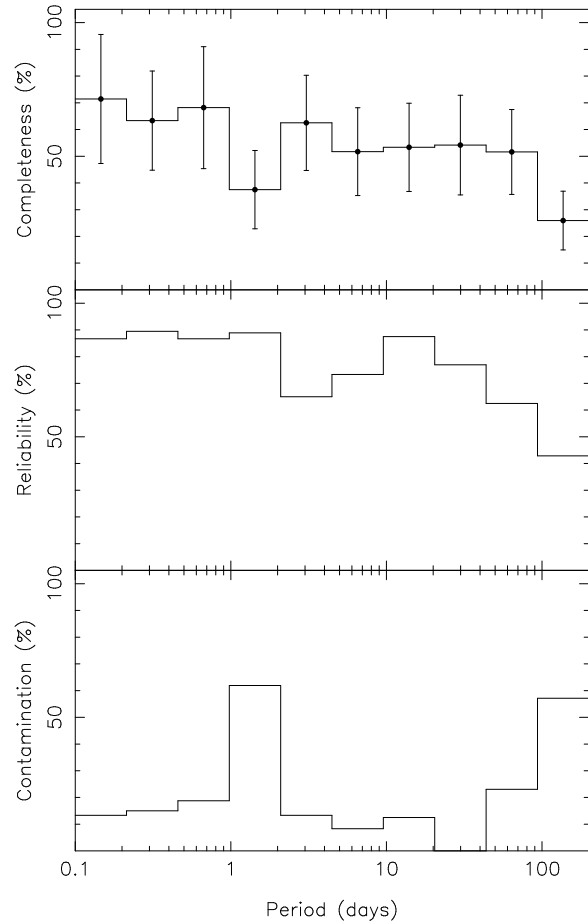


FIG. 4.— Results of the simulations for 0.005 mag semi-amplitude expressed as percentages, plotted as a function of period. **Top panel:** completeness as a function of real (input) period. **Center panel:** Reliability of period determination, plotted as the fraction of objects with a given true period, detected with the correct period (defined as differing by  $< 10\%$  from the true period). **Bottom panel:** Contamination, plotted as the fraction of objects with a given detected period, having a true period differing by  $> 10\%$  from the detected value.

in the completeness statistic between the two bins: this merely counts detections, without regard to whether the period was correctly determined.

While it is important to perform the simulation on M-dwarf target stars to account for the systematics, it is expected that in reality, many or even the majority of these should show real, astrophysical variability at some level. It is therefore likely that we have injected our simulated signals into objects which also have astrophysical signals. For the 0.01 mag amplitude, this does not appear to be a serious problem, with the injected signal generally overwhelming anything already present. However, this could contribute to explaining the apparently high contamination and the lack of a significant drop in completeness in the 0.005 mag amplitude sample.

In order to investigate these effects, and in particular to also test the influence of systematics on the detection rate, we have performed an additional set of simulations for 0.005 mag semi-amplitude but using white, Gaussian noise of standard deviation set by the estimated observational errors, rather than using the observed light curves. This procedure eliminates systematics (“correlated noise”) and any existing astrophysical variability but should otherwise have a comparable noise level to

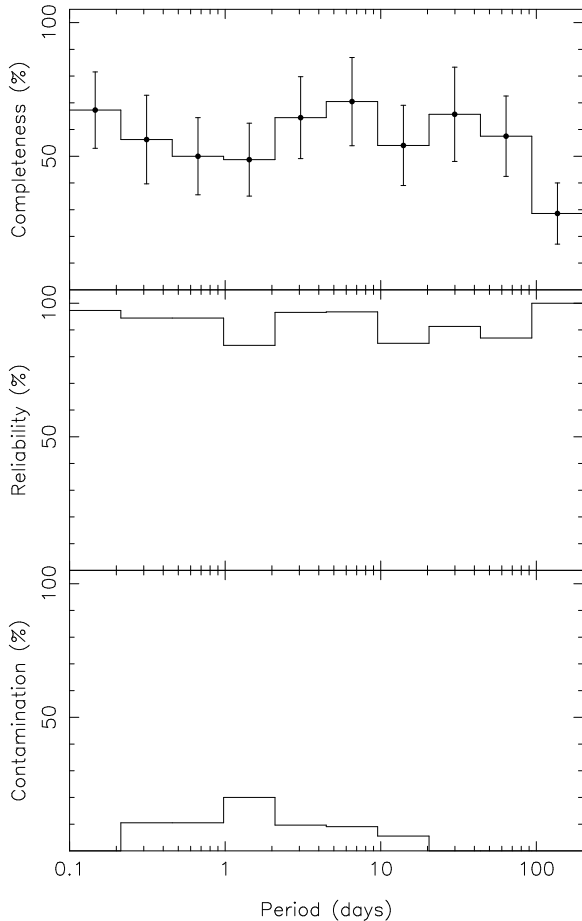


FIG. 5.— Panels as Figure 4 except for 0.01 mag semi-amplitude.

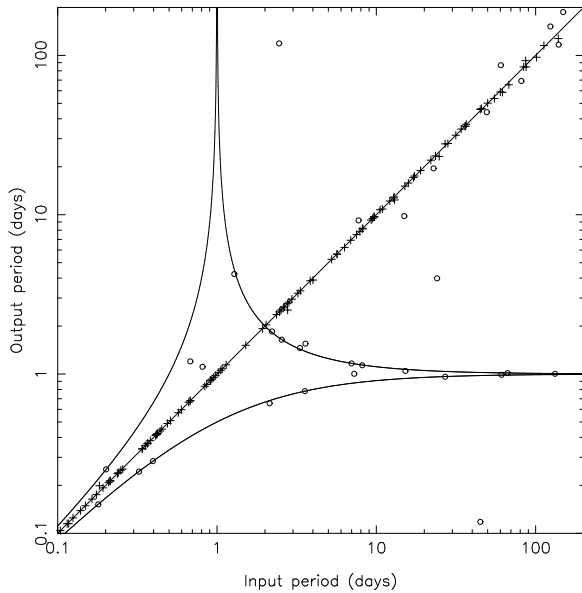


FIG. 6.— Recovered period as a function of actual period for our simulations at 0.005 mag semi-amplitude. Crosses represent objects where the correct period was recovered to within 10%, and open circles show objects failing this criterion. The diagonal line indicates equal periods, and the curves show the loci of the 1 day<sup>-1</sup> aliases.

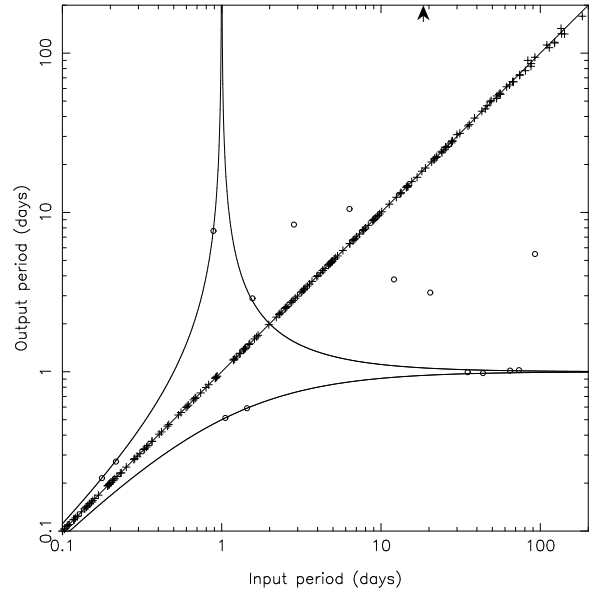


FIG. 7.— Recovered period as a function of actual period for our simulations at 0.01 mag semi-amplitude. Symbols and lines as Figure 6. The arrow at the top of the diagram indicates a single point which fell outside the plotted range.

the real data. The results are shown in Figure 8. This indicates that the low completeness seen in Figures 4 and 5 at short periods results from a roughly equal contribution of systematics (or contamination from variability) and other effects (sampling and noise). The completeness at long periods is slightly improved, but as expected, is still lower than at short periods, remaining at the  $\approx 50\%$  level. This is most likely due to the sampling. The contamination and reliability histograms show a substantial improvement, with close to ideal period recovery, which suggests these effects are almost entirely due to systematics (or contamination from variability).

#### 4. RESULTS

Our results are presented in Table 1, and the phase-folded light curves of all 41 objects are shown in Figure 9.

It is evident from Figure 9 that the light curves for several objects (e.g. LHS 1068, G 32-37A, GJ 170, LHS 543a) are not perfectly sinusoidal. This is indeed expected if the modulations arise from stellar spots. It is also important to note that there exist pathological spot distributions (e.g. two identical active longitudes spaced by  $180^\circ$ ) which can lead to doubling (or in the general case, multiplication by an integer) of the frequency, causing us to mis-estimate true the rotation period of the star. One way to check for this is to compare the rotation periods with  $v \sin i$  measurements.

We have searched for literature measurements of radial and rotational velocities for our targets, finding  $v \sin i$  measurements for 8 objects (Delfosse et al. 1998; Mohanty & Basri 2003; Browning et al. 2010). These are summarized in Table 2, which includes radial velocities and kinematic population assignments for two additional objects (Montes et al. 2001).

Figure 10 shows a comparison of these  $v \sin i$  measurements with the rotation velocities inferred from our period measurements and radius estimates. These are generally in good agreement, with the exception of one object, LP412-31. This is one of the latest-type objects in

TABLE 2  
ROTATIONAL VELOCITIES, RADIAL VELOCITIES AND KINEMATIC POPULATIONS  
FROM THE LITERATURE FOR OUR TARGETS

Name	$v \sin i$ (km s <sup>-1</sup> )	$\sigma(v \sin i)$ (km s <sup>-1</sup> )	$v_{\text{rad}}$ (km s <sup>-1</sup> )	Population <sup>a</sup>	Reference <sup>b</sup>
GJ51	...	...	4.4	YD	1
GJ1057	< 2.2	...	27	OD	2
LP412-31	12.0	2.0	48.8	YD	3
G099-049	7.39	0.8	30	YD	2
LHS1885	< 3.7	...	16	YO	2
GJ285	4.6	0.4	26.5	YD	4
GJ1156	9.2	1.9	4	YD	2
GJ493.1	16.8	2.1	-27	YD	2
GJ791.2	32.0	2.0	-29	YD	2
GJ856A	...	...	-24	YD?	1

<sup>a</sup> See Leggett (1992).

<sup>b</sup> (1) Montes et al. (2001); (2) Delfosse et al. (1998); (3) Mohanty & Basri (2003); (4) Browning et al. (2010)

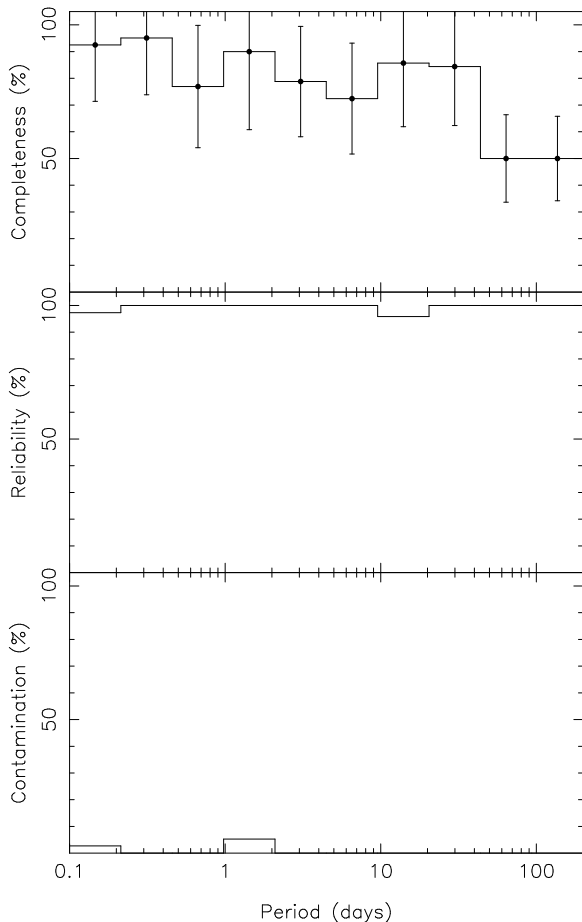


FIG. 8.— Panels as Figure 4 except simulating light curves with white, Gaussian noise rather than using real data.

our sample (Mohanty & Basri 2003 state a spectral type of M8.0), so we suspect the discrepancy may be caused by an error in the assumed radius when calculating  $v_{\text{rot}}$ , especially noting the lack of objects at these late spectral types in the Ribas (2006) sample we used to derive the empirical mass-radius relation.

#### 4.1. Kinematic population and age assignment

It is important for the analysis of rotational evolution (performed later in this section) to be able to assign ap-

proximate ages to the MEarth sample. This is a notoriously difficult problem for field stars. For the purposes of the present work, we use the available kinematic information (5 of the 6 phase-space dimensions, where we lack radial velocities for the majority of the targets) to statistically assign our targets to the Galactic thin disk or thick disk / halo populations.

Previous studies have used tangential velocity (e.g. Reiners & Basri 2008), but this does not take into account the bulk motions of the various Galactic populations along each line of sight through the Galaxy. Instead, we use the model of Dhital et al. (2010) to compute the predicted mean proper motions and their dispersion for the Galactic thin disk at the position of each M-dwarf, and compare to the measured proper motions. Stars within  $< 1\sigma$  of the thin disk prediction were labeled “thin” (likely thin disk members), stars at  $> 3\sigma$  were labeled “thick” (corresponding to the thick disk / halo) and are likely to be old, and the intermediate cases were labeled “mid”. These population assignments are reported in Table 1.

We have assigned a 0.5 – 3 Gyr age to the “thin” stars, and a 7 – 13 Gyr age to the “thick” stars (e.g., Feltzing & Bensby 2008). The “mid” sample in reality contains a mixture of thin and thick disk populations, so we assign it an intermediate age of 3 – 7 Gyr.

#### 4.2. Rotation period distribution

Figure 11 shows rotation period plotted as a function of stellar mass, where the symbols indicate our kinematic population assignments from §4.1. This diagram shows no clear trend of rotation period with stellar mass. The population appears to be in two main clumps in the diagram, a population of very rapidly rotating objects with periods of  $\approx 0.2$ –10 days, and a population of very slowly rotating objects with periods of 30 days to the sensitivity limit of the observations at approximately 150 days.

The “thin” sample falls entirely within the rapidly rotating clump of objects, whereas the majority of the “thick” stars fall in the slowly-rotating clump. The situation is intermediate between these extremes for the “mid” sample. Given the likely ages of these populations, this indicates that the older objects in the sample are on average rotating more slowly. Such a trend is a natural consequence of the expectation that these stars spin

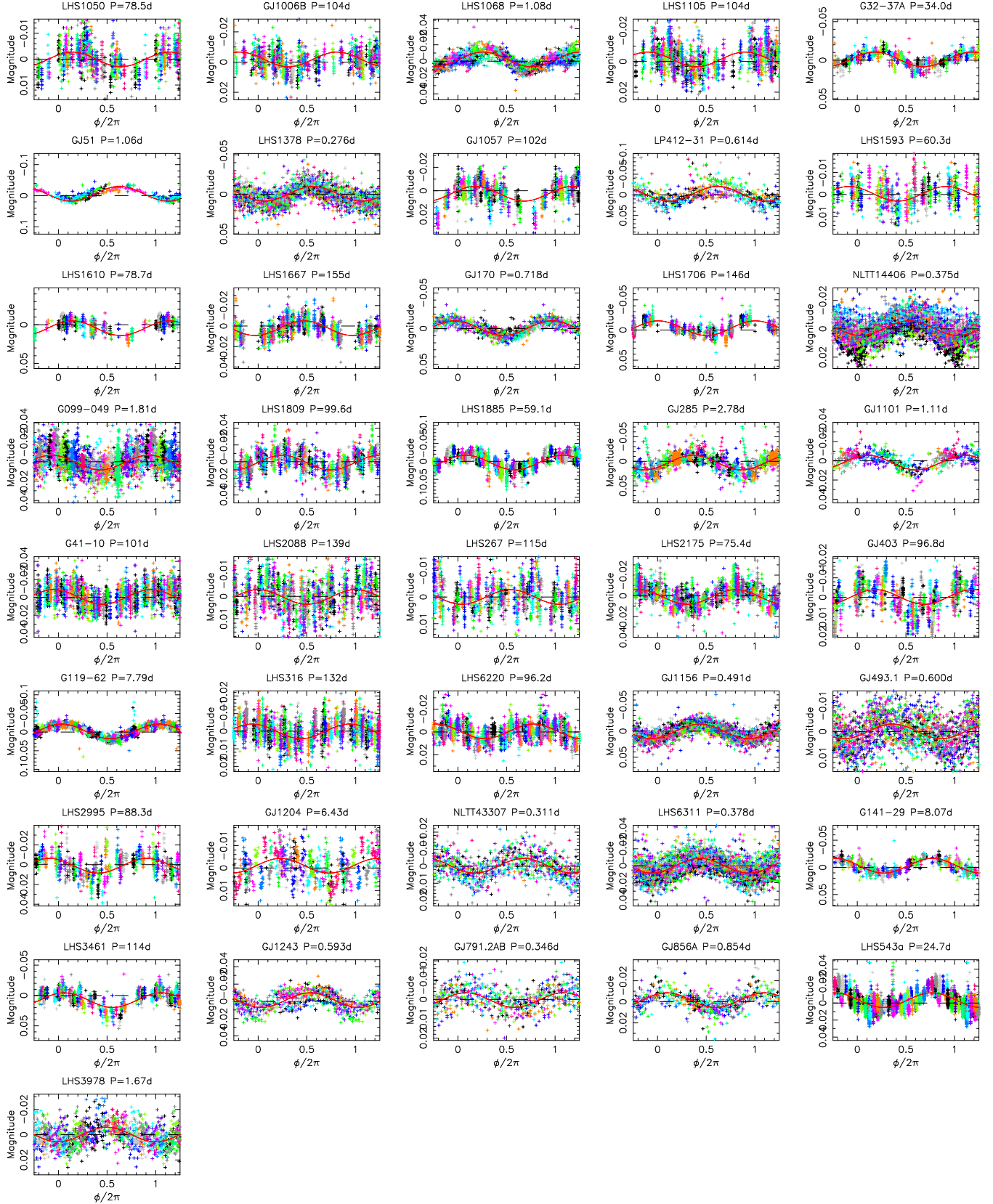


FIG. 9.— Phase-folded light curves for our 41 rotation candidates. Differential magnitudes are plotted, in the MEarth instrumental system. In these diagrams, we plot  $\phi/2\pi$  on the horizontal axis, where  $\phi$  is defined in Eq. (2), and have subtracted the “meridian correction” and “common mode correction” described in the text.



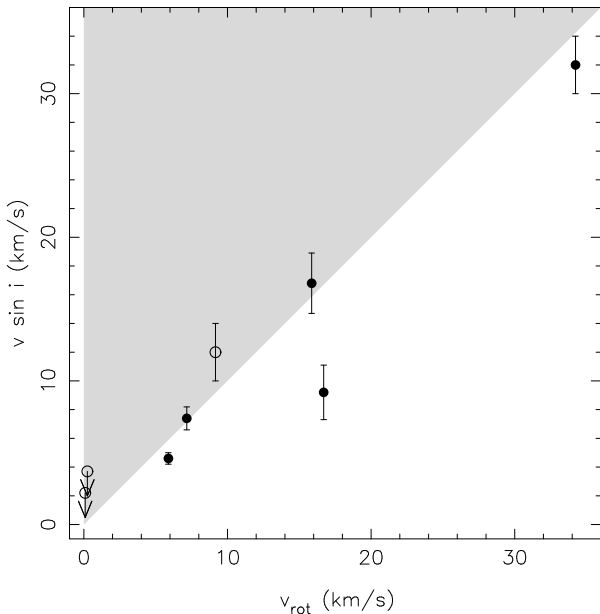


FIG. 10.—  $v \sin i$  from spectroscopic measurements plotted as a function of rotation velocity from our period measurements, assuming the stellar radii given in Table 1. Points with arrows show the two  $v \sin i$  limits. Open symbols denote young/old (YO) and old disc (OD) objects, and filled symbols denote young disc (YD). The gray shaded region indicates the part of the diagram where  $v \sin i > v_{\text{rot}}$ , and should not be occupied. Note that the stellar radii (and thus the estimated rotation velocities) also have significant uncertainties, but these are difficult to quantify, so we have not plotted horizontal error bars on the diagram. These uncertainties are likely to amount to at least 10%, and probably greater given the uncertainties in the effects of activity on M-dwarf radii (e.g. Chabrier et al. 2007).

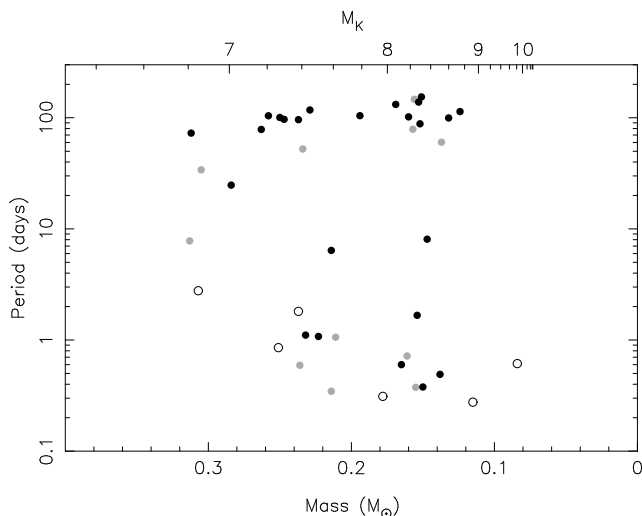


FIG. 11.— Rotation period as a function of stellar mass for our sample. The symbols indicate our kinematic population assignments: open circles indicate “thin” objects (likely thin disk and hence younger), gray filled circles “mid” objects, and black filled circles indicate “thick” objects (likely thick disk or halo and hence older).

down due to winds as they age, and the lack of slowly rotating stars in the “thin” sample compared to the abundance of them in the “thick” sample further indicates that this spin-down takes place during ages intermediate between these two samples for the majority of the M-dwarfs. These conclusions confirm the findings of the  $v \sin i$  studies (e.g. Delfosse et al. 1998; Reiners & Basri

TABLE 3  
LIST OF REFERENCES FOR ROTATION PERIODS FROM THE LITERATURE.

Cluster	Age (Myr)	Source(s)
ONC	1	Herbst et al. (2001, 2002) Stassun et al. (1999)
NGC 2264	2	Lamm et al. (2005) Makidon et al. (2004)
NGC 2362	5	Irwin et al. (2008b)
IC 2391	30	Patten & Simon (1996)
IC 2602		Barnes et al. (1999)
NGC 2547	40	Irwin et al. (2008a)
Pleiades	100	Hartman et al. (2009a) Terndrup et al. (1999) Scholz & Eislöffel (2004b)
NGC 2516	150	Irwin et al. (2007b)
M35	150	Meibom et al. (2009)
Hyades	625	Radick et al. (1987) Prosser et al. (1995)
Praesepe	650	Scholz & Eislöffel (2007)
Field		Baliunas, Sokoloff & Soon (1996) Barnes (2001, 2003) Kiraga & Stępień (2007) Benedict et al. (1998)

2008).

Using a two-sided Kolmogorov-Smirnov test, we have verified that the difference between the “thin” and “thick” periods is statistically significant, with a probability of  $4 \times 10^{-3}$  that these are drawn from the same parent population. The corresponding probabilities for the “thin” and “mid”, and the “mid” and “thick” pairs, are 0.13 and 0.06, respectively, neither of which we consider to be statistically significant. This is not surprising as the sample sizes are quite small and the “mid” population likely consists of a mixture of the other two populations. The median periods are 0.7, 7.8, and 92 days for the “thin”, “mid” and “thick” samples, respectively.

## 5. DISCUSSION

### 5.1. Morphological comparison with open cluster data

In Figure 12 (see Table 3 for a list of data sources) we show Figure 11 in the wider context of rotation period distributions from the literature for younger stars in open clusters, and for more massive stars in the field.

For the M-Earth sample, we have assumed the “thin” population and “young disc” are equivalent, and likewise for “thick” and “old disc”. The “mid” objects are plotted in both panels using open symbols as it is not clear to which population these should be assigned, and it is likely the “mid” sample contains members of both, with the slower rotating objects being more likely to belong to the “old disc” population and vice versa.

Figure 12 shows that the pre-main-sequence behavior of M-dwarfs is markedly different from that of solar-type stars. The open cluster data indicate that the M-dwarfs all appear to spin up rapidly, and reach very rapid rotation rates at 100 – 200 Myr age, which corresponds to the time at which the most massive objects in the  $< 0.35 M_{\odot}$  domain reach the ZAMS. Furthermore, the slowest rotation period seen at any given mass is itself a very strong function of mass, declining moving to less massive objects. The similar morphologies in the diagrams, especially from NGC 2264 to NGC 2516 (after

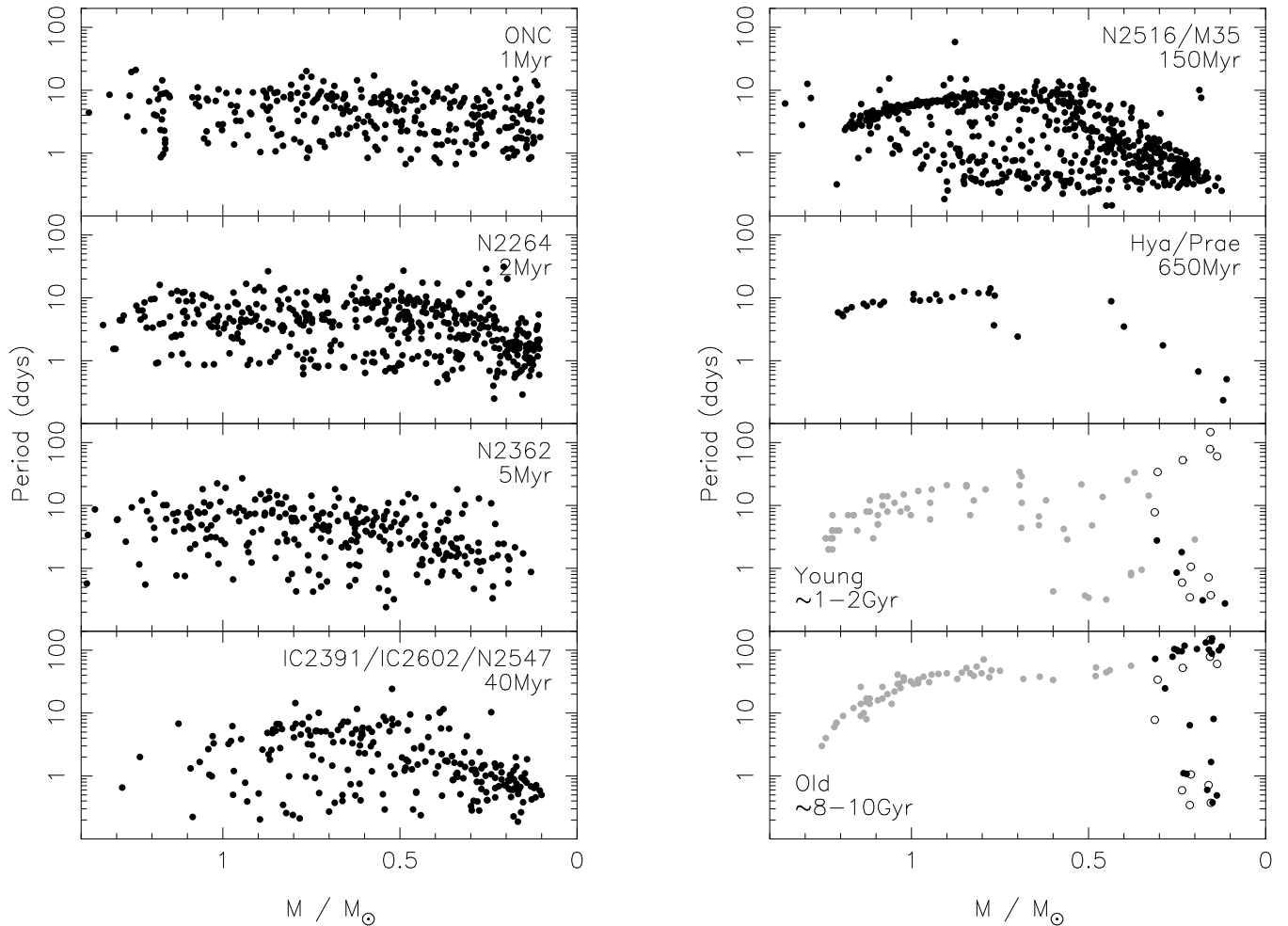


FIG. 12.— Compilation of rotation periods for low-mass stars from the literature, including the results from the present study. Plotted in each panel is rotation period as a function of stellar mass for a single cluster, or several clusters that are close to coeval. In the case of the field star samples, we divided them into two bins for the “young disc” and “old disc” stars, respectively, and color all the literature data gray to distinguish them from the results of the present study (in black). We plot the “thin” population in the “young” panel and the “thick” population in the “old” panel, both as solid symbols, with the “mid” population shown in both panels using open symbols (see text). Measurements for field stars are from the compilation by Barnes (2001, 2003) of the rotation periods for the Mount Wilson stars from Baliunas, Sokoloff & Soon (1996), down to  $\approx 0.7 M_{\odot}$ , Kiraga & Stepień (2007) for early-M dwarfs, and the present study for later objects. The appropriate references for each panel are given in Table 3. All the masses for the cluster samples were computed using the I-band luminosities of the sources and the models of Baraffe et al. (1998), assuming values of the age, distance modulus and reddening for the clusters taken from the literature. For the field stars, the Delfosse et al. (2000) mass-absolute magnitude relations were used for M-dwarfs, and for all higher-mass stars, we converted the observed  $B - V$  colors to effective temperature using Table A5 from Kenyon & Hartmann (1995), and then to mass using the models of Baraffe et al. (1998).

accounting for the expected spin-up due to contraction, which corresponds simply to a vertical translation in this logarithmic plot), indicate there is relatively little rotation rate dependence in the PMS evolution.

Between the Pleiades age ( $\approx 100$  Myr from isochrone fitting; Meynet, Mermilliod & Maeder 1993) clusters and the much older Praesepe cluster, the available data indicate there is essentially no evolution of the rotation period, so it appears that little angular momentum is lost over this phase of the evolution, corresponding to the arrival at the ZAMS and the early main sequence for these stars. It is, however, important to note that the available samples at the Hyades/Praesepe age are very limited at the present time, so we must caution drawing strong conclusions from them. We shall return to this point later in the discussion.

While the M-dwarfs do not appear to have spun down at the age of the Hyades/Praesepe, this process is clearly well underway for the earlier M-dwarfs by the “young

disc” age, and apparently complete by the “old disc” age above approximately  $0.4 M_{\odot}$ . Below this mass, there is a dramatic change moving from the “young disc” sample to the “old disc” sample (especially recalling the uncertainty as to which bin the “mid” objects, plotted as open symbols, should be assigned), where many slowly rotating stars are now found, but there is still a wide range of rotation periods here, in contrast to the higher masses, spanning about 2 orders of magnitude.

It is interesting, and suggestive, to compare the rotation period distribution in the lower right panel of Figure 12 with the activity fraction (e.g. Fig. 3 of West et al. 2008). The fraction of active field M-dwarfs shows a steep rise around M5 spectral types. It is at approximately this point moving down in mass where the rapid rotation phenomenon appears at the oldest ages. Given the age range displayed in the diagram, this seems most likely to be an evolutionary effect: the time at which the stars spin down increases with decreasing mass, becoming comparable to

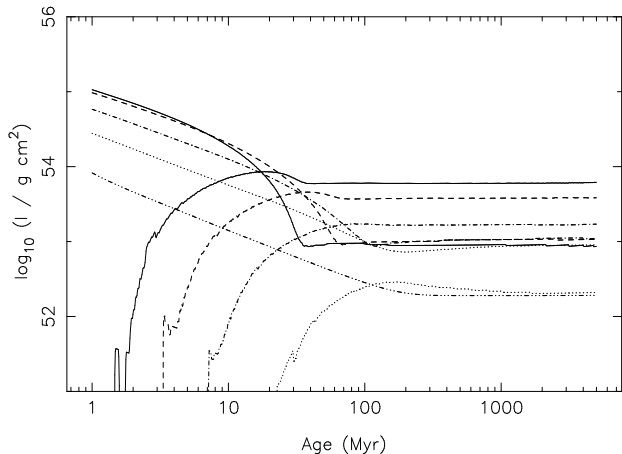


FIG. 13.— Evolution of the moment of inertia from the models of Baraffe et al. (1998) for the radiative core (lower lines) and convective envelope (upper lines) for masses of 1.0 (solid line), 0.8 (dashed line), 0.6 (single dot dashed line), 0.4 (dotted line), and 0.2  $M_{\odot}$  (triple dot dash line). Note that the 0.2  $M_{\odot}$  star does not form a radiative core so only one line is shown.

the sample age below the fully-convective boundary.

The existence of a wide range in rotation rates, and the appearance of a substantial number of slow rotators below the fully-convective boundary moving between our “thin” and “thick” bins (although some are also evident in the “mid” bin) further suggests that any spin-down occurs quite rapidly in the interval between the nominal ages of these samples for the majority of fully-convective objects, i.e. around 5 Gyr in age.

These timescales are in good agreement with those of West et al. (2008), e.g. their Fig. 10, where they find activity lifetimes of  $\approx 7$  Gyr below the fully-convective boundary, and  $\lesssim 2$  Gyr for the partially-radiative objects above it. We shall explore possibilities for generating such a spin-down in terms of wind models in §5.2.

We note some morphological features in the diagram for the “old disc” sample. The highest mass stars show the familiar break in the Kraft (1967) curve around 1.2  $M_{\odot}$ , which is thought to be due to the disappearance of the surface convective zones moving to higher masses. Stars without surface convective zones appear to experience no (or very little) wind losses on the main sequence and thus remain at very rapid rotation rates until they start to evolve off the main sequence.

There is another discontinuity in the diagrams around 0.5 – 0.6  $M_{\odot}$ , which is highly evident in the NGC 2516 distribution, and has been noticed and discussed by many authors. We note here that the Kiraga & Stępień (2007) sample appears to also show a discontinuity at this mass for field M-dwarfs, where the rotation period has relatively little mass dependence immediately above this mass, and appears to increase with decreasing mass below it.

## 5.2. Rotational evolution models

Figure 14 gives an alternative presentation of the available rotation period data for objects below 0.35  $M_{\odot}$ , in a way where the evolution is more explicit, at the expense of the mass information seen in the period versus mass plots. It is important to bear in mind the strong mass dependence, particularly in the open cluster samples, when trying to interpret this figure. We have assigned ages to the MEarth sample based on the discussion in §4.1, not-

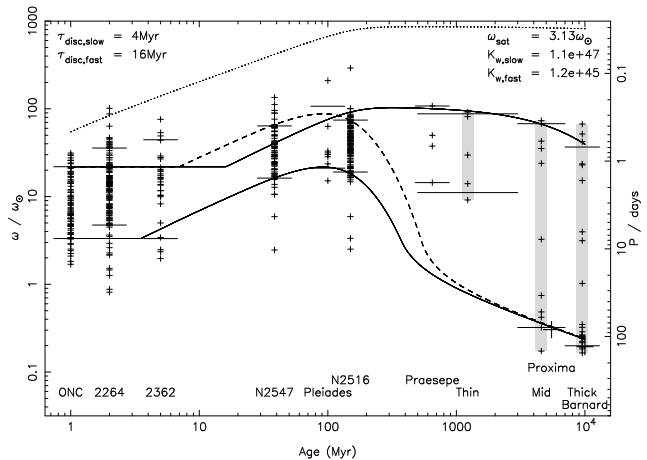


FIG. 14.— Rotational angular velocity  $\omega$  plotted as a function of time for stars with masses  $0.1 < M/M_{\odot} \leq 0.35$ . Crosses show the rotation period data such that each cluster (or field sample) collapses into a vertical stripe on the diagram, and short horizontal lines show the 10th and 90th percentiles of  $\omega$ , used to characterize the slow and fast rotators respectively. Plotted are the ONC, NGC 2264, NGC 2362, NGC 2547, the Pleiades, NGC 2516, Praesepe, and the MEarth data. We also show the positions of Proxima and Barnard’s star from Benedict et al. (1998) as the large, bold crosses. We have assigned ages to the field stars for the purposes of plotting them on this diagram, assuming 6 Gyr for Proxima (the center of the range of ages published for the  $\alpha$  Cen system; e.g. Guenther & Demarque 2000; Eggenberger 2004), 10 Gyr for Barnard’s star, and 0.5 – 3 Gyr for the “thin”, 3 – 7 Gyr for the “mid”, and 7 – 12 Gyr for the “thick” MEarth samples (see §4.1). These age ranges for the MEarth samples are indicated by the lengths of the horizontal lines displaying the percentiles, and the MEarth data are shaded gray. The solid curves show rotational evolution models for 0.25  $M_{\odot}$  stars, fit to the percentiles, Proxima and Barnard’s star, with the upper curve for the rapid rotators (with parameters  $\tau_{\text{disc,fast}}$  and  $K_{w,\text{fast}}$ ) and the lower curve for the slow rotators (parameters  $\tau_{\text{disc,slow}}$  and  $K_{w,\text{slow}}$ ). The dashed curve shows the result for the rapid rotators if the wind parameter ( $K_{w,\text{fast}}$ ) is assumed to be the same as for the slow rotators rather than allowing it to vary. The dotted curve shows the break-up limit from Eq. (5).

ing that in reality, there is a large spread in age for each of the bins.

In order to model the evolution, we follow the method of Bouvier, Forestini & Allain (1997). We adopt a standard wind prescription commonly used for solar-type stars (e.g., Chaboyer, Demarque & Pinsonneault 1995; Barnes & Sofia 1996), using a modified version of the Kawaler (1988) wind law with  $a = 1$  and  $n = 3/2$ , introducing saturation of the angular velocity dependence at a critical angular velocity  $\omega_{\text{sat}}$ :

$$\left(\frac{dJ}{dt}\right)_{\text{wind}} = \begin{cases} -K_w \omega^3 \left(\frac{R}{R_{\odot}}\right)^{1/2} \left(\frac{M}{M_{\odot}}\right)^{-1/2}, & \omega < \omega_{\text{sat}} \\ -K_w \omega \omega_{\text{sat}}^2 \left(\frac{R}{R_{\odot}}\right)^{1/2} \left(\frac{M}{M_{\odot}}\right)^{-1/2}, & \omega \geq \omega_{\text{sat}} \end{cases} \quad (3)$$

By coupling this wind prescription to a stellar evolution model, here the Lyon NEXTGEN models of Baraffe et al. (1998), we model the full evolution of the angular velocity  $\omega$  as a function of time. This model has several free parameters. We assume an initial angular velocity  $\omega_0$ , here fixed to the observed velocities in the ONC, and this is held constant for a time  $\tau_{\text{disc}}$  to account for disc-related angular momentum losses (“disc locking”) on the earliest parts of the pre-main-sequence. The slow and fast rotator branches are allowed to assume

different values of both of these parameters, with the expectation that the fastest rotators should decouple from their discs earlier than the slower rotators. For the fully-convective objects modeled here, we treat the stars as solid bodies. The subsequent evolution is then governed only by the two parameters  $K_w$  and  $\omega_{\text{sat}}$ , which control the normalization of the wind losses and the saturation rate, respectively.

For a solar-type star,  $K_w$  can be calibrated by forcing the model to reproduce the observed rotation rate of the Sun. For M-dwarfs there is as yet no analogous object with an old, well-determined age and rotation period (although Proxima comes closest to providing it), and indeed the rotation rates of the slow and fast rotator branches appear to not yet have converged even by the oldest ages we consider, so instead we simply fit for this parameter.

Saturation is thought to occur when the rotation period becomes much smaller than the convective overturn time (e.g., Krishnamurthi et al. 1997). These authors introduced a scaling of  $\omega_{\text{sat}}$  with mass, of the form:

$$\omega_{\text{sat}} = \omega_{\text{sat},\odot} \frac{\tau_{\odot}}{\tau_c} \quad (4)$$

where  $\tau_c$  is the convective overturn timescale at 200 Myr. The convective overturn time lengthens for lower mass stars, resulting in  $\omega_{\text{sat}}$  decreasing with decreasing stellar mass (corresponding to slower rotation).

Typical values of  $\omega_{\text{sat}}$  adopted by other authors for the masses we consider here (0.25  $M_{\odot}$ ) are of order a few times the (present-day) solar angular velocity (e.g., Sills, Pinsonneault & Terndrup 2000), corresponding to periods of a few to ten days.

It is important to note that the convective overturn timescales are not well-known for fully-convective stars; Sills et al. (2000) extrapolated the theoretical values from Kim & Demarque (1996) to these masses, and found that the resulting values of  $\omega_{\text{sat}}$  caused too much angular momentum to be lost compared to the observations in the Hyades, which were better reproduced with a smaller value of  $\omega_{\text{sat}}$ . More recent studies of empirical convective overturn timescales (Pizzolato et al. 2003; Kiraga & Stępień 2007) indicate that  $\tau_c$  may increase sharply around the fully-convective boundary, meaning such an extrapolation might under-predict  $\tau_c$ , and thus overpredict  $\omega_{\text{sat}}$ , as found. It is also possible that the Rossby number is no longer the dominant factor in determining the operation of the magnetic dynamo driving stellar winds in fully-convective objects (e.g. Mohanty & Basri 2003; Reiners & Basri 2007).

The uncertainties associated with the Rossby scaling have led us to consider several possibilities for  $\omega_{\text{sat}}$ . We first consider a value close to that of Sills et al. (2000). We then allow essentially free adjustment of  $\omega_{\text{sat}}$  (§5.2.2), and finally consider a third possibility of there being no un-saturated regime, for comparison, in §5.2.3.

### 5.2.1. High $\omega_{\text{sat}}$ model

If we start by enforcing values of  $\omega_{\text{sat}}$  of a few  $\omega_{\odot}$ , the model shown in Figure 14 results. We have performed two fits, one enforcing the same value of  $K_w$  for both the fast and slow rotator branches, as would be expected in the saturation formalism for solar-type stars, and one allowing different values of  $K_w$ . We consider first the

former model, enforcing the same value of  $K_w$  for both branches.

This model is able to reproduce the cluster slow rotators fairly well, and the oldest ages (Proxima, Barnard’s star, and the “thick” MEarth sample). The disagreement with the Praesepe sample and the “thin” sample is more concerning, although we note that the age range of the latter in practice means it could contain objects as young as the Hyades/Praesepe, and that the “thick” and “mid” samples could contain objects as young as a few Gyr as well. This model does not reproduce the rapid spin-down at late times discussed in §5.1.

In the case of the Hyades/Praesepe this model would predict that there should be objects rotating as slowly as the sun by this age. There are to our knowledge no such objects reported in the literature at the present time, but we suspect the majority of cluster studies carried out at these masses and ages are not sensitive to periods this long. For example, Scholz & Eislöffel (2007) state that their sensitivity to periods longer than 1 week is limited.

The situation for the rapid rotators is much less satisfactory, with difficulties reproducing the data during both the early-PMS and the main sequence phases. We first examine the latter.

As for solar-type stars, the wind prescription we have used produces a rapid convergence in rotation rates at late times. This does not seem to be the case for M-dwarfs. If we instead allow a different value of  $K_w$  for the fast rotators, corresponding to allowing the normalization of the wind law to be rotation rate dependent, it is possible to much better reproduce the observations from the age of NGC 2516 onwards. The value of  $K_w$  found here is two orders of magnitude smaller than that for the slow rotator branch: these objects experience much weaker winds in our model.

The theoretical interpretation of such a change likely lies in the dynamo mechanism operating in these objects, as mentioned in §1. Of the possibilities mentioned there, the  $\alpha^2$  dynamo would possess a strong rotation rate dependence, for example.

We now return to the question of the early-PMS evolution of the rapid rotators. Figure 14 shows that, contrary to the slow rotators, these objects appear to spin up more slowly than would be predicted simply from contraction. Since the stellar evolution model we are using has no rotation rate dependence, our model would only be able to reproduce such an evolution by losing angular momentum at early-times, in this case by choosing a very long disc coupling time of 16 Myr. This seems physically unreasonable (and still does not fit the data), especially recalling that the rapid rotators are thought to be produced from stars which uncoupled from their discs early.

It is possible the prescription for disc locking we have used, of a constant angular velocity, is not correct, and a more gradual angular momentum removal operates. This could result in reduced (rather than eliminated) spin-up. The slow rotators do not seem to support this, showing apparently relatively little evolution as measured by the percentiles out to ages of 5 Myr. It is however important to note that the slow rotation end of the samples is subject to contamination from field objects, so it is possible this conclusion is a result of the higher level of field contamination in the NGC 2362 sample, compared

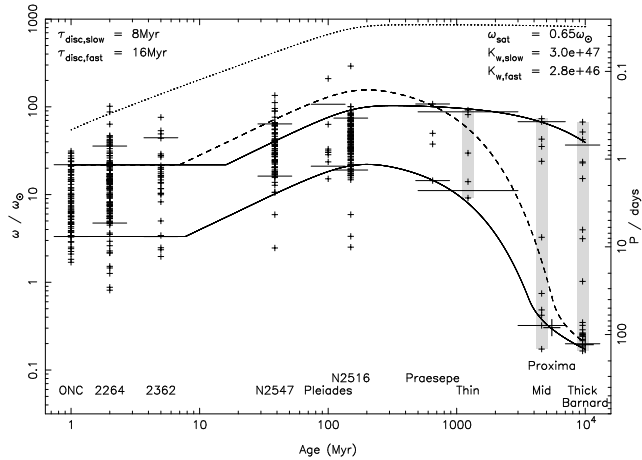


FIG. 15.— As Figure 14, except for low values of  $\omega_{\text{sat}}$ .

to the ONC and NGC 2264.

Another possible clue may be the proximity of these objects to the break-up limit. Herbst et al. (2001) give the following formula for the period corresponding to break-up:

$$P_{\text{break}} = 0.116 \text{ days} \frac{(R/R_{\odot})^{3/2}}{(M/M_{\odot})^{1/2}} \quad (5)$$

where  $M$  and  $R$  are the stellar mass and radius, respectively. This is plotted as the dotted line on Figure 14. As stated by Herbst et al. (2001), many of these objects are indeed rotating very close to the break-up rate, with many approaching 30% of break-up. This appears to persist to ages of approximately 10 Myr.

In reality, the proximity of these objects to the break-up limit means the non-rotating stellar evolution model we have used may no longer be applicable, because it implies centrifugal forces are likely to play an important role in determining the stellar structure. It may therefore be necessary to invoke a more complete treatment of stellar evolution, incorporating rotation, to reproduce the behavior of these objects, for example the treatment used by Sills et al. (2000) and Denissenkov et al. (2010).

#### 5.2.2. Low $\omega_{\text{sat}}$ model

If we relax the assumption made in §5.2.1 of a value of  $\omega_{\text{sat}}$  of a few  $\omega_{\odot}$ , it is possible to obtain an alternate solution which better-fits the behavior at late times, at the cost of worse agreement with the open cluster data around the age of the Pleiades. We show this solution in Figure 15, which has  $\omega_{\text{sat}} = 0.65 \omega_{\odot}$ .

This model appears more satisfactory overall, especially considering the age ranges in the field samples, and the strong mass-dependence and possible field contamination in the open cluster samples, meaning some scatter for the slow rotators in such a wide mass bin is not entirely unexpected. The values of the wind parameter  $K_w$  still differ for the fast and slow rotator branches, but now by only one order of magnitude. The rapid spin-down at late times discussed in §5.1 is now produced.

#### 5.2.3. Zero $\omega_{\text{sat}}$ model

Reiners & Basri (2008) have offered an interpretation of the available  $v \sin i$  data in terms of a saturated wind braking law, with a temperature dependence yielding

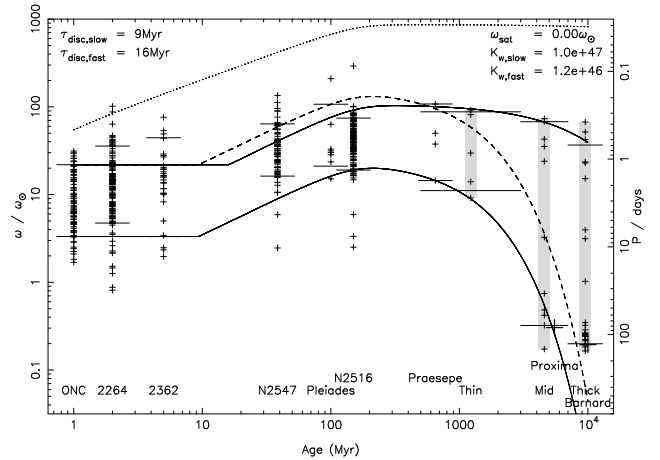


FIG. 16.— As Figure 14, except assuming all objects remain in the saturated regime throughout their evolution.

weaker angular momentum losses for lower-mass objects. In their analysis, they assume all the objects rotate faster than the saturation rate, corresponding to elimination of the  $dJ/dt \propto -\omega^3$  branch in Eq. (3). This could also correspond, for example, to a different magnetic dynamo than the solar-type objects have at low rotation rates.

After the object arrives on the main sequence, the moment of inertia and temperature are approximately constant for a given star, so this angular momentum loss prescription can be trivially integrated to show that the angular velocity is an exponential function of time. This drives the object very quickly to extremely low rotation rate. In the context of Figure 14, where both axes are logarithmic, this law corresponds to an exponential decrease in  $\log \omega$  versus  $\log t$ .

Nonetheless, given the limited quantity of data available it is possible to obtain a somewhat satisfactory fit using this model, as shown in Figure 16.

#### 5.2.4. Overall comments

The first two models we have considered in this section both exhibit a non-saturated spin-down at late-times on the slow rotator branch, with the periods evolving following a  $t^{1/2}$  law as for solar-type stars. While we have essentially enforced the solar-type law by our choice of wind prescription, it is important to note that, in reality, different power laws may be possible depending on the exact magnetic geometry. Nonetheless this argues in favor of a phase of “non-saturated” angular momentum losses. Some observational evidence in favor of fully-convective M-dwarfs being able to support a non-saturated dynamo exists in the form of a possible rotation-activity correlation (e.g., Delfosse et al. 1998; Mohanty & Basri 2003; although see also West & Basri 2009).

We note that the period of  $\approx 130$  days measured for Barnard’s star by Benedict et al. (1998) may also argue in favor of a  $t^{1/2}$  or similarly slow spin-down at late times, and thus against the model in §5.2.3. Although the evidence for such a periodicity is stated by Benedict et al. (1998) themselves as being weak, the MEarth sample contains similarly long periods. Barnard’s star appears to be a thick disc object, and thus is likely to have an age of approximately 7–13 Gyr (e.g., Feltzing & Bensby 2008). If we assume Proxima and Barnard’s star can be treated as evolutionary analogs, the ratio of rota-

tion periods of 0.64 is remarkably close to the predicted  $1/\sqrt{2} \simeq 0.71$  from a  $t^{1/2}$  law if Barnard’s star was twice as old as Proxima. The exponential spin-down in Figure 16 would produce a much larger change in period.

Finally, the “pile-up” of objects at long periods seen in the MEarth data is difficult to reproduce with an exponential time-dependence in the late-time evolution. The convergence in rotation rates produced by the transition to a  $t^{1/2}$  type spin-down law more naturally produces this feature, whereas the exponential spin-down instead produces a divergence in periods at late-times when we use the wind parameter variation with rotation rate in §5.2.3.

Given these lines of reasoning, we believe the model in §5.2.3 is unlikely, and further has the somewhat unsatisfactory feature of producing extreme slow rotators ( $\gtrsim 1000$  days) at the oldest ages (see also the discussion in Reiners & Basri 2008).

Of the remaining two models, we suggest that the observed spin-down at late-times (see §5.1) and the activity lifetimes (West et al. 2008) support the model presented in §5.2.2. A comparison of Figures 14 and 15 indicates that the largest differences between these two possibilities (noting that the age range and small number statistics for the “thin” sample does not strongly constrain the model at present) are manifest at the age of the Hyades and/or Praesepe, with one model predicting the existence of objects rotating as slowly as the sun, and the other being consistent with the presently-available observations. More generally, the slowest rotation period seen at this age constrains the value of  $\omega_{\text{sat}}$ . We believe these arguments motivate extending the observations to search for slowly rotating M-dwarfs in these clusters.

## 6. CONCLUSIONS

We have presented a sample of rotation period measurements for 41 field M-dwarfs inferred to lie below the fully-convective boundary, from the MEarth transit survey. We measure a wide range of periods, from 0.28 days to 154 days, where the latter is commensurate with the sensitivity limit resulting from the typical baseline of the observations, finding that the kinematically young (thin disk) objects rotate faster than the kinematically old (thick disk) objects.

Combining the available measurements from the literature with the present sample shows two interesting features in the mass dependence of rotation for M-dwarfs at the oldest field ages. One is the familiar discontinuity at approximately  $0.6 M_{\odot}$  seen in many open cluster studies, where the mass-dependence of the rotation periods steepens below this mass. Contrary to the findings of the open cluster studies, the field stars below  $0.6 M_{\odot}$  appear to rotate *slower* with decreasing mass.

The second feature is the onset (moving down in mass) of rapid rotation at old ages for some objects below  $0.35 M_{\odot}$ , which is also seen in the  $v \sin i$  surveys. Our rotation periods confirm that not all such field M-dwarfs are rapid rotators, and there exists a significant, or even dominant, population of slow rotators that appears between the ages corresponding to our thin and thick disk samples. In addition to this confirmation of the results of  $v \sin i$  studies (e.g. Delfosse et al. 1998), we can now estimate the rotation rates for the slow rotators, finding them to rotate approximately two orders of magnitude

slower than the remaining rapidly rotating objects at the age corresponding to our thick disk sample. There is no discontinuity in the rotation rates crossing  $0.35 M_{\odot}$  for the slow rotator branch at the oldest ages.

Comparing the results for the partially-radiative and fully-convective objects indicates that the spin-down time increases moving to lower masses. The “young disk” sample from Kiraga & Stępień (2007) has a comparable fraction of rapid rotators to the “mid” and “thick” samples from the present survey, indicating that the spin-down times for these populations are comparable to the respective sample ages: the “young disk” sample age for the partly-radiative stars (a few Gyr) and the thick / “old disk” (probably  $> 5$  Gyr) for the fully-convective stars.

We have explored wind models and were able to reproduce these features by adopting a very low saturation velocity within a standard (Chaboyer et al. 1995; Barnes & Sofia 1996) wind prescription, although it was necessary to assume a rather large rotation rate dependence of the wind parameter. In reality, this additional rotation rate dependence probably corresponds to modifying the power law exponent  $n$  in the wind model, and thus the magnetic field geometry, although it is beyond the scope of this paper to speculate on such a change.

The MEarth team gratefully acknowledges funding from the David and Lucile Packard Fellowship for Science and Engineering (awarded to DC). This material is based upon work supported by the National Science Foundation under grant number AST-0807690. We thank Saurav Dhital for computing the Galactic model results along the sight-lines to our M-dwarfs, Isabelle Baraffe for providing the stellar evolution model tracks used in §5.2 and for discussion of the location of the fully-convective boundary as a function of time, and Jerome Bouvier, Marc Pinsonneault and Alexander Scholz for assistance with the rotational evolution models and for helpful discussions regarding the interpretation. The anonymous referee is also thanked for a helpful report that significantly improved the manuscript. The MEarth team is greatly indebted to the staff at the Fred Lawrence Whipple Observatory for their efforts in construction and maintenance of the facility, and would like to explicitly thank Wayne Peters, Ted Groner, Karen Erdman-Myres, Grace Alegria, Rodger Harris, Bob Hutchins, Dave Martina, Dennis Jankovsky and Tom Welsh for their support.

This research has made extensive use of data products from the Two Micron All Sky Survey, which is a joint project of the University of Massachusetts and the Infrared Processing and Analysis Center / California Institute of Technology, funded by NASA and the NSF, NASA’s Astrophysics Data System (ADS), and the SIMBAD database, operated at CDS, Strasbourg, France.

## REFERENCES

- Allain, S. 1998, *A&A*, 333, 629
- Angione, R. J. 1999, in *ASP Conf. Ser.* 189, Precision CCD Photometry, ed. E. R. Craine, D. L. Crawford, & R. A. Tucker (San Francisco, CA: ASP), 16
- Bailer-Jones, C. A. L., & Lamm, M. 2003, *MNRAS*, 339, 477
- Baliunas, S., Sokoloff, D., & Soon, W. 1996, *ApJ*, 457, 99
- Baraffe, I., Chabrier, G., Allard, F. & Hauschildt, P. H. 1998, *A&A*, 337, 403
- Barnes, S. & Sofia, S. 1996, *ApJ*, 462, 746
- Barnes, S. A., Sofia, S., Prosser, C. F., & Stauffer, J. R. 1999, *ApJ*, 516, 263
- Barnes, S. A. 2001, *ApJ*, 561, 1095
- Barnes, S. A. 2003, *ApJ*, 586, 464
- Barnes, S. A. 2007, *ApJ*, 669, 1167
- Benedict, G. F., et al. 1998, *AJ*, 116, 429
- Benedict, G. F., McArthur, B. E., Franz, O. G., Wasserman, L. H., & Henry, T. J. 2000, *AJ*, 120, 1106
- Bouvier, J., Forestini, M., & Allain, S. 1997, *A&A*, 326, 1023
- Browning, M. K., Basri, G., Marcy, G. W., West, A. A., Zhang, J. 2010, *AJ*, 139, 504
- Chaboyer, B., Demarque, P., & Pinsonneault, M. H. 1995, *ApJ*, 441, 865
- Chabrier, G., & Baraffe, I. 1997, *A&A*, 327, 1039
- Chabrier, G., Gallardo, J., Baraffe, I. 2007, *A&A*, 472, 17
- Charbonneau, D. 2009, *Nature*, 462, 891
- Cieza, L. & Baliber, N. 2006, *ApJ*, 649, 862
- Cohen, R. E., Herbst, W., & Williams, E. C. 2004, *AJ*, 127, 1602
- Collier Cameron, A., Campbell, C. G. & Quaintrell, H. 1995, *A&A*, 298, 133
- Dahn, C. C., et al. 2002, *AJ*, 124, 1170
- Delfosse, X., Forveille, T., Perrier, C. & Mayor, M. 1998, *A&A*, 331, 581
- Delfosse, X., Forveille, T., Ségransan, D., Beuzit, J.-L., Udry, S., Perrier, C. & Mayor, M. 2000, *A&A*, 364, 217
- Denissenkov, P. A., Pinsonneault, M., Terndrup, D. M. & Newsham, G. 2010, *ApJ*, 716, 1269
- Dhital, S., West, A. A., Stassun, K. G. & Bochanski, J. J. 2010, *ApJ*, 139, 2566
- Donati, J.-F., et al. 2008, *MNRAS*, 390, 545
- Durney, B. R., De Young, D. S. & Roxburgh, I. W. 1993, *Sol. Phys.*, 145, 207
- Eggenberger, P., Charbonnel, C., Talon, S., Meynet, G., Maeder, A., Carrier, F., & Bourban, G. 2004, *A&A*, 417, 253
- Elias, J. H., Frogel, J. A., Matthews, K., & Neugebauer, G. 1982, *AJ*, 87, 1029
- Elias, J. H., Frogel, J. A., Hyland, A. R., & Jones, T. J. 1983, *AJ*, 88, 1027
- Feltzing, S., & Bensby, T. 2008, in *Physica Scripta*, 133, A stellar journey, ed. P. Barklem, A. Korn, & B. Plez, 4031
- Geunther, D. B., & Demarque, P. 2000, *ApJ*, 531, 503
- Hartman, J. D., et al. 2009a, *ApJ*, 691, 342
- Hartman, J. D., Bakos, G. Á., Noyes, R. W., Sipöcz, B., Kovács, G., Mazeh, T., Shporer, A. & Pál, A. 2009b, *AJ*, submitted ([arXiv:0907.2924](https://arxiv.org/abs/0907.2924))
- Herbst W., Bailer-Jones C. A. L., & Mundt R. 2001, *ApJ*, 554, 197
- Herbst W., Bailer-Jones C. A. L., Mundt R., Meisenheimer K., & Wackermann R. 2002, *A&A*, 396, 513
- Irwin, J., Aigrain, S., Hodgkin, S., Irwin, M., Bouvier, J., Clarke, C., Hebb, L., & Moraux, E. 2006, *MNRAS*, 370, 954
- Irwin, J., Irwin, M., Aigrain, S., Hodgkin, S., Hebb, L., & Moraux, E. 2007a, *MNRAS*, 375, 1449
- Irwin, J., Hodgkin, S., Aigrain, S., Hebb, L., Bouvier, J., Clarke, C., Moraux, E. & Bramich, D. M. 2007b, *MNRAS*, 377, 741
- Irwin, J., Hodgkin, S., Aigrain, S., Bouvier, J., Hebb, L. & Moraux, E. 2008a, *MNRAS*, 383, 1588
- Irwin, J., Hodgkin, S., Aigrain, S., Bouvier, J., Hebb, L. Irwin, M. & Moraux, E. 2008b, *MNRAS*, 384, 675
- Irwin, J., Charbonneau, D., Nutzman, P., & Falco E. 2009, in *IAU Symp.* 253, Transiting Planets, ed. F. Pont, D. Sasselov, & M. Holman (Cambridge: Cambridge Univ. Press), 37
- Kawaler, S. D. 1998, *ApJ*, 333, 236
- Kenyon, S. J. & Hartmann L. 1995, *ApJS*, 101, 117
- Kim, Y.-C., & Demarque, P. 1996, *ApJ*, 457, 340
- Kiraga, M. & Stepień, K. 2007, *Acta Astron.*, 57, 149
- Königl, A. 1991, *ApJ*, 370, L37
- Kraft, R. P. 1967, *ApJ*, 150, 551
- Krishnamurthi, A., Pinsonneault, M. H., Barnes, S. & Sofia, S. 1997, *ApJ*, 480, 303
- Lamm M. H., Mundt R., Bailer-Jones C. A. L., & Herbst W. 2005, *A&A*, 430, 1005
- Leggett, S. K. 1992, *ApJS*, 82, 351
- Lépine, S., & Shara, P. 2005, *AJ*, 129, 1483
- Lépine, S. 2005, *AJ*, 130, 1680
- Littlefair, S. P., Naylor, T., Burningham, B., & Jeffries, R. D. 2005, *MNRAS*, 358, 341
- Littlefair, S. P., Naylor, T., Mayne, N. J., Saunders, E. S., & Jeffries, R. D. 2010, *MNRAS*, 403, 545
- Makidon, R. B., Rebull, L. M., Strom, S. E., Adams, M. T., & Patten, B. M. 2004, *AJ*, 127, 2228
- Matt, S. & Pudritz, R. E. 2005, *ApJ*, 632, 135
- Meibom, S., Mathieu, R. D., & Stassun, K. G. 2009, *ApJ*, 695, 679
- Meynet, G., Mermilliod, J.-C., & Maeder, A. 1993, *A&AS*, 98, 477
- Mohanty, S. & Basri, G. 2003, *ApJ*, 583, 451
- Montes, D., López-Santiago, E., Gálvez, M. C., Fernández-Figueroa, M. J., De Castro, J. & Cornide, M. 2001, *MNRAS*, 328, 45
- Morin, J., et al. 2008, *MNRAS*, 390, 567
- Morin, J., Donati, J. F., Petit, P., Delfosse, X., Forveille, T., & Jardine, M. M. 2010, *MNRAS*, in press ([arXiv:1005.5552](https://arxiv.org/abs/1005.5552))
- Nutzman, P. & Charbonneau, D. 2008, *PASP*, 120, 317
- Patten, B. M. & Simon, T. 1996, *ApJS*, 106, 489
- Perryman, M. A. C., et al. 1997, *The Hipparcos and Tycho Catalogues* (ESA SP-1200; Noordwijk: ESA)
- Perryman, M. A. C., Brown, A. G. A., Lebreton, Y., Gomez, A., Turon, C., de Strobel, G. C., Mermilliod, J.-C., Robichon, N., Kovalevsky, J., & Crifo, F. 1998, *A&A*, 331, 81
- Pizzolato, N., Maggio, A., Micela, G., Sciortino, S., & Ventura, P. 2003, *A&A*, 397, 147
- Prosser, C. F., et al. 1995, *PASP*, 107, 211
- Radick, R. R., Thompson, D. T., Lockwood, G. W., Duncan, D. K., & Baggett, W. E. 1987, *ApJ*, 321, 459
- Rädler, K.-H., Wiedemann, E., Brandenburg, A., Meinel, R., & Tuominen, I. 1990, *A&A*, 239, 413
- Reiners, A. & Basri, G. 2007, *ApJ*, 656, 1121
- Reiners, A. & Basri, G. 2008, *ApJ*, 684, 1390
- Reiners, A. & Basri, G. 2009, *A&A*, 496, 787
- Ribas, I. 2006, *Ap&SS*, 304, 89
- Scholz, A. & Eislöffel, J. 2004a, *A&A*, 419, 249
- Scholz, A. & Eislöffel, J. 2004b, *A&A*, 421, 259
- Scholz, A. & Eislöffel, J. 2005, *A&A*, 429, 1007
- Scholz, A. & Eislöffel, J. 2007, *MNRAS*, 381, 1638
- Scholz, A., Eislöffel, J., & Mundt, R. 2009, *MNRAS*, 400, 1548
- Sills, A., Pinsonneault, M. H., & Terndrup, D. M. 2000, *ApJ*, 534, 335
- Stassun, K. G., Mathieu, R. D., Mazeh, T., & Vrba, F. J. 1999, *AJ*, 117, 2941
- Stauffer, J. R. & Hartmann, L. W. 1987, *ApJ*, 318, 337
- Terndrup, D. M., Krishnamurthi, A., Pinsonneault, M. H., & Stauffer, J. R. 1999, *AJ*, 118, 1814
- van Altena, W. F., Lee, J. T., & Hoffleit, E. D. 1995, *The General Catalogue of Trigonometric Stellar Parallaxes* (4th ed.; New Haven: Yale Univ. Obs.)
- West, A. A., Hawley, S. L., Bochanski, J. J., Covey, K. R., Reid, I. N., Dhital, S., Hilton, E. J. & Masuda, M. 2008, *AJ*, 135, 785
- West, A. A., & Basri, G. 2009, *ApJ*, 693, 1283
- Zahn J.-P. 1977, *A&A*, 57, 383

TABLE 1  
 ROTATION PERIODS, KINEMATICS AND STELLAR PARAMETERS FOR THE MEARTH  
 SAMPLE.

Name	$\alpha^a$ ICRS	$\delta^a$ ICRS	Epoch <sup>a</sup> (yr)	$\mu_\alpha^b$ ("'/yr)	$\mu_\delta^b$ ("'/yr)	$\pi$ (")	$\sigma(\pi)$ (")	Ref. <sup>c</sup>	$K^d$ (mag)	$M^e$ ( $M_\odot$ )	$R^f$ ( $R_\odot$ )	Period <sup>g</sup> (days)	$a^h$ (mag)	Pop <sup>i</sup>
LHS1050	00 <sup>h</sup> 15 <sup>m</sup> 49 <sup>s</sup> .2	+13°33'22''	1998.7	0.621	0.333	0.0866	0.0134	1	7.83	0.26	0.28	78.5	0.0028	Thick
GJ1006B	00 <sup>h</sup> 16 <sup>m</sup> 16 <sup>s</sup> .1	+19°51'52''	1998.7	0.709	-0.748	0.0660	0.0016	2	8.12	0.26	0.28	104	0.0049	Thick
LHS1068	00 <sup>h</sup> 24 <sup>m</sup> 34 <sup>s</sup> .8	+30°02'30''	1997.9	0.580	0.028	0.0528	0.0044	1	8.91	0.22	0.24	1.08	0.0090	Thick
LHS1105	00 <sup>h</sup> 35 <sup>m</sup> 53 <sup>s</sup> .6	+52°41'37''	1998.9	0.787	-0.186	0.0621	0.0091	1	9.81	0.19	0.21	104	0.0048	Thick
G32-37A	00 <sup>h</sup> 39 <sup>m</sup> 33 <sup>s</sup> .5	+14°54'19''	1997.8	0.321	0.039	0.0353	0.0018	1	9.14	0.30	0.32	34.0	0.0095	Mid
GJ51	01 <sup>h</sup> 03 <sup>m</sup> 19 <sup>s</sup> .7	+62°21'56''	1999.0	0.739	0.086	0.0955	0.0073	1	7.74	0.21	0.23	1.06	0.0236	Mid
LHS1378	02 <sup>h</sup> 17 <sup>m</sup> 09 <sup>s</sup> .9	+35°26'33''	1998.0	0.549	-0.266	0.0964	0.0011	1	9.03	0.12	0.14	0.276	0.0093	Thin
GJ1057	03 <sup>h</sup> 13 <sup>m</sup> 23 <sup>s</sup> .0	+04°46'29''	2000.7	1.749	0.084	0.1171	0.0035	3	7.85	0.16	0.18	102	0.0062	Thick
LP412-31	03 <sup>h</sup> 20 <sup>m</sup> 59 <sup>s</sup> .7	+18°54'23''	1997.8	0.351	-0.259	0.0689	0.0006	4	10.66	0.08	0.11	0.613	0.0188	Thin
LHS1593	03 <sup>h</sup> 47 <sup>m</sup> 20 <sup>s</sup> .9	+08°41'46''	2000.9	0.465	-0.664	0.0795	0.0035	1	9.04	0.14	0.16	60.3	0.0033	Mid
LHS1610	03 <sup>h</sup> 52 <sup>m</sup> 41 <sup>s</sup> .7	+17°01'06''	1997.8	0.433	-0.644	0.0700	0.0138	1	8.07	0.16	0.18	78.8	0.0099	Mid
LHS1667	04 <sup>h</sup> 22 <sup>m</sup> 33 <sup>s</sup> .5	+39°00'44''	1999.9	0.584	-0.603	0.0534	0.0047	1	9.69	0.15	0.17	154	0.0071	Thick
GJ170	04 <sup>h</sup> 30 <sup>m</sup> 25 <sup>s</sup> .3	+39°51'00''	1998.9	0.271	-0.575	0.0959	0.0028	1	8.26	0.16	0.18	0.718	0.0103	Mid
LHS1706	04 <sup>h</sup> 50 <sup>m</sup> 50 <sup>s</sup> .8	+22°07'22''	1997.8	0.636	-0.433	0.0711	0.0057	1	8.99	0.16	0.18	147	0.0121	Mid
NLTT14406	05 <sup>h</sup> 03 <sup>m</sup> 05 <sup>s</sup> .6	+21°22'36''	1997.8	0.109	-0.140	0.0365	0.0084	1	8.91	0.15	0.18	0.375	0.0050	Mid
G099-049	06 <sup>h</sup> 00 <sup>m</sup> 03 <sup>s</sup> .5	+02°42'24''	1999.8	0.311	-0.042	0.1862	0.0101	3	6.06	0.24	0.26	1.81	0.0076	Thin
LHS1809	06 <sup>h</sup> 02 <sup>m</sup> 29 <sup>s</sup> .2	+49°51'56''	2000.1	0.058	-0.861	0.1077	0.0026	3	8.45	0.13	0.16	99.6	0.0088	Thick
LHS1885	06 <sup>h</sup> 57 <sup>m</sup> 57 <sup>s</sup> .0	+62°19'20''	1999.0	0.327	-0.516	0.0874	0.0023	1	7.71	0.23	0.25	52.4	0.0239	Mid
GJ285	07 <sup>h</sup> 44 <sup>m</sup> 40 <sup>s</sup> .2	+03°33'09''	1999.9	-0.348	-0.447	0.1686	0.0027	2	5.72	0.31	0.32	2.78	0.0150	Thin
GJ1101	07 <sup>h</sup> 55 <sup>m</sup> 54 <sup>s</sup> .0	+83°23'05''	1999.9	-0.291	-0.604	0.0803	0.0030	1	7.93	0.23	0.25	1.11	0.0076	Thick
G41-10	08 <sup>h</sup> 58 <sup>m</sup> 12 <sup>s</sup> .7	+19°43'49''	1998.8	-0.427	0.096	0.0332	0.0046	1	9.76	0.25	0.27	101	0.0082	Thick
LHS2088	08 <sup>h</sup> 59 <sup>m</sup> 56 <sup>s</sup> .1	+72°57'36''	1999.3	0.973	-0.035	0.0726	0.0034	1	8.99	0.15	0.18	138	0.0033	Thick
LHS267	09 <sup>h</sup> 20 <sup>m</sup> 57 <sup>s</sup> .9	+03°22'06''	2000.1	0.316	-1.139	0.0608	0.0041	1	8.54	0.23	0.25	118	0.0027	Thick
LHS2175	09 <sup>h</sup> 42 <sup>m</sup> 23 <sup>s</sup> .3	+55°59'02''	1999.0	-0.703	-0.517	0.0651	0.0087	1	7.55	0.31	0.33	72.8	0.0069	Thick
GJ403	10 <sup>h</sup> 52 <sup>m</sup> 04 <sup>s</sup> .4	+13°59'51''	1998.0	-1.115	0.198	0.0839	0.0257	1	7.81	0.25	0.27	96.8	0.0038	Thick
G119-62	11 <sup>h</sup> 11 <sup>m</sup> 51 <sup>s</sup> .8	+33°32'11''	1998.4	-0.164	0.110	0.0683	0.0106	1	7.51	0.31	0.33	7.79	0.0197	Mid
LHS316	11 <sup>h</sup> 50 <sup>m</sup> 57 <sup>s</sup> .9	+48°22'40''	1999.0	-1.540	-0.960	0.1221	0.0029	3	7.66	0.17	0.19	132	0.0042	Thick
LHS6220	12 <sup>h</sup> 05 <sup>m</sup> 29 <sup>s</sup> .7	+69°32'23''	1999.2	-0.447	-0.040	0.0602	0.0134	1	7.91	0.24	0.26	96.2	0.0064	Thick
GJ1156	12 <sup>h</sup> 18 <sup>m</sup> 59 <sup>s</sup> .4	+11°07'34''	2000.2	-1.263	0.199	0.1529	0.0030	3	7.59	0.14	0.16	0.491	0.0142	Thick
GJ493.1	13 <sup>h</sup> 00 <sup>m</sup> 33 <sup>s</sup> .5	+05°41'08''	2000.2	-0.934	0.215	0.1231	0.0035	3	7.68	0.17	0.19	0.600	0.0028	Thick
LHS2995	14 <sup>h</sup> 53 <sup>m</sup> 37 <sup>s</sup> .2	+11°34'12''	2000.3	0.076	-0.738	0.0535	0.0041	1	9.67	0.15	0.17	88.3	0.0074	Thick
GJ1204	16 <sup>h</sup> 36 <sup>m</sup> 05 <sup>s</sup> .6	+08°48'49''	2000.4	-0.519	-0.151	0.0652	0.0042	1	8.53	0.21	0.23	6.41	0.0033	Thick
NLTT43307	16 <sup>h</sup> 40 <sup>m</sup> 06 <sup>s</sup> .0	+00°42'19''	2000.3	0.174	-0.163	0.0890	0.0023	1	8.23	0.18	0.20	0.311	0.0043	Thin
LHS6311	16 <sup>h</sup> 40 <sup>m</sup> 20 <sup>s</sup> .7	+67°36'05''	1999.4	-0.262	0.361	0.0747	0.0043	1	8.97	0.15	0.17	0.378	0.0091	Thick
G141-29	18 <sup>h</sup> 42 <sup>m</sup> 45 <sup>s</sup> .0	+13°54'17''	1999.4	-0.025	0.347	0.0933	0.0115	1	7.57	0.15	0.17	8.07	0.0132	Thick
LHS3461	19 <sup>h</sup> 24 <sup>m</sup> 16 <sup>s</sup> .3	+75°33'12''	2000.4	0.374	0.591	0.0903	0.0051	1	8.98	0.12	0.15	114	0.0121	Thick
GJ1243	19 <sup>h</sup> 51 <sup>m</sup> 09 <sup>s</sup> .3	+46°29'00''	1998.4	0.188	0.266	0.0841	0.0024	1	7.79	0.24	0.26	0.593	0.0085	Mid
GJ791.2AB <sup>j</sup>	20 <sup>h</sup> 29 <sup>m</sup> 48 <sup>s</sup> .4	+09°41'20''	2000.4	0.665	0.132	0.1138	0.0019	3	7.33	0.21	0.23	0.346	0.0038	Mid
GJ856A	22 <sup>h</sup> 23 <sup>m</sup> 29 <sup>s</sup> .0	+32°27'33''	1998.5	0.255	-0.208	0.0622	0.0100	2	6.07	0.25	0.27	0.854	0.0070	Thin
LHS543a	23 <sup>h</sup> 25 <sup>m</sup> 40 <sup>s</sup> .2	+53°08'06''	1998.9	0.986	0.328	0.0404	0.0031	1	9.00	0.28	0.30	24.8	0.0077	Thick
LHS3978	23 <sup>h</sup> 35 <sup>m</sup> 41 <sup>s</sup> .3	+06°11'21''	2000.7	0.566	0.268	0.0416	0.0032	1	10.19	0.15	0.18	1.67	0.0055	Thick



TABLE 1  
 ROTATION PERIODS, KINEMATICS AND STELLAR PARAMETERS FOR THE MEARTH  
 SAMPLE.

- <sup>a</sup> Coordinates from 2MASS, epoch of measurement as specified in the “epoch” column.
- <sup>b</sup> From Lépine & Shara (2005).
- <sup>c</sup> Reference for parallax measurement: (1) Yale Parallax Catalog, van Altena et al. (1995); (2) The *Hipparcos* catalog, Perryman et al. (1997); (3) NASA NStars database (<http://nstars.arc.nasa.gov/>); (4) Dahn et al. (2002). Compiled by Lépine (2005).
- <sup>d</sup> From 2MASS, converted to the CIT system of Elias et al. (1982, 1983) using the transformation from the 2MASS explanatory supplement.
- <sup>e</sup> Using the *K*-band absolute magnitude and the relation of Delfosse et al. (2000).
- <sup>f</sup> Derived from *M* using a polynomial fit to the empirical mass-radius data of Ribas (2006).
- <sup>g</sup> While we have not attempted to estimate formal period uncertainties, our simulations indicate that the uncertainty in the periods is  $< 1\%$  for  $P < 10$  d,  $\approx 1\%$  for  $10 \leq P < 20$  days,  $2\%$  for  $20 \leq P < 50$  days,  $5 - 10\%$  for  $50 \leq P < 100$  days, and  $20 - 30\%$  for  $P \geq 100$  days.
- <sup>h</sup> Semi-amplitude of modulation seen in the MEarth bandpass.
- <sup>i</sup> Kinematic population, see §4.1.
- <sup>j</sup> Visual binary, unresolved in these observations; see Benedict et al. (2000).